

pubs.acs.org/acscatalysis Research Article

# Catalytic Reduction of Aqueous Chlorate With $MoO_x$ Immobilized on Pd/C

Changxu Ren, Peng Yang, Jinyu Gao, Xiangchen Huo, Xiaopeng Min, Eric Y. Bi, Yiming Liu, Yin Wang, Mengqiang Zhu, and Jinyong Liu\*



Cite This: ACS Catal. 2020, 10, 8201-8211



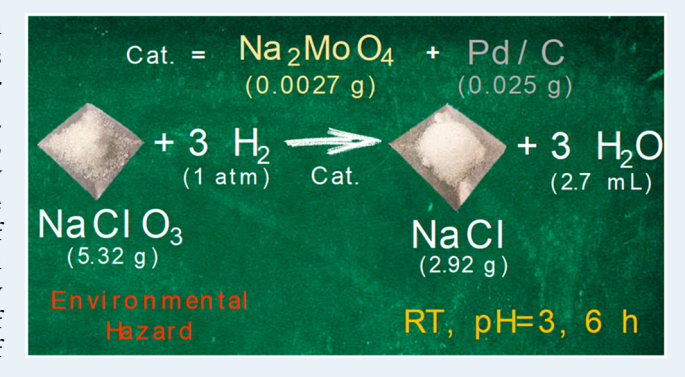
**ACCESS** 

III Metrics & More

Article Recommendations

Supporting Information

**ABSTRACT:** Chlorate (ClO $_3^-$ ) is an undesirable byproduct in the chlor-alkali process. It is also a heavily used chemical in various industrial and agricultural applications, making it a toxic water pollutant worldwide. Catalytic reduction of ClO $_3^-$  into Cl $^-$  by H $_2$  is of great interest to both emission control and water purification, but platinum group metal catalysts are either sluggish or severely inhibited by halide anions. Here, we report on the facile preparation, robust performance, and mechanistic investigation of a MoO $_x$ -Pd/C catalyst for aqueous ClO $_3^-$  reduction. Under 1 atm H $_2$  and room temperature, the Na $_2$ MoO $_4$  precursor is rapidly immobilized from aqueous solution onto Pd/C as a mixture of low-valent Mo oxides. The catalyst enables complete reduction of ClO $_3^-$  in a wide concentration range (e.g., 1  $\mu$ M to 1 M) into Cl $^-$ .



The addition of Mo to Pd/C not only enhances the catalytic activity by >55-fold, but also provides strong resistance to concentrated salts. To probe the reaction mechanisms, we conducted a series of kinetic measurements, microscopic and X-ray spectroscopic characterizations, sorption experiments, tests with other oxyanion substrates, and a comparative study using dissolved Mo species. The catalytic sites are the reduced  $MoO_x$  species (primarily  $Mo^{IV}$ ), showing selective and proton-assisted reactivity with  $ClO_3^-$ . This work demonstrates a great promise of using relatively abundant metals to expand the functionality of hydrogenation catalysts for environmental and energy applications.

KEYWORDS: chlorate reduction, brine electrolysis, water purification, molybdenum, palladium, oxygen atom transfer, X-ray photoelectron spectroscopy, X-ray absorption spectroscopy

## ■ INTRODUCTION

Catalytic reduction of toxic chlorate (ClO<sub>3</sub><sup>-</sup>) has significant values for both industrial sustainability and environmental protection. More than 4 million tons of KClO<sub>3</sub> are manufactured worldwide each year by the electrochemical chlorate process.<sup>1,2</sup> Heavy uses of chlorate in various industrial and agricultural applications (e.g., pulp bleaching, weed control, pyrotechnics, and water disinfection) have led to widespread environmental pollution<sup>3</sup> and emerging challenges for water systems.<sup>4</sup> The World Health Organization (WHO) has proposed a guideline for limiting the ClO<sub>3</sub><sup>-</sup> concentration below 0.7 mg L<sup>-1</sup> in drinking water. The third Unregulated Contaminant Monitoring Rule (UCMR 3) by the United States Environmental Protection Agency (USEPA) included ClO<sub>3</sub><sup>-</sup> as a contaminant monitored by public water systems, with the Minimum Reporting Level at 0.02 mg L<sup>-1.5</sup> On the other hand, the global production of Cl<sub>2</sub> has reached over 70 million tons per year by the electrochemical chlor-alkali process, where on average one kg of ClO<sub>3</sub><sup>-</sup> is generated per ton of Cl<sub>2</sub> produced. The undesirable ClO<sub>3</sub><sup>-</sup> byproduct has negative effects on both the manufacturing processes and the

environment. <sup>6,10</sup> Hence, at least 70 000 tons of ClO<sub>3</sub><sup>-</sup> must be treated in chlor-alkali plants per year. Typical waste brines from the chlor-alkali process contain up to 10 g L<sup>-1</sup> of ClO<sub>3</sub><sup>-</sup> and up to 5 M of NaCl. <sup>6,10,11</sup> Other emerging electrochemical technologies such as water splitting, <sup>12</sup> wastewater treatment, <sup>13</sup> and direct HCl production from seawater desalination waste brines <sup>14</sup> also produce various levels of undesirable ClO<sub>3</sub><sup>-</sup> at the anode. <sup>7,8</sup> Therefore, an efficient and robust approach for ClO<sub>3</sub><sup>-</sup> reduction is beneficial for a wide scope of industrial and environmental endeavors.

In chlor-alkali plants, the  $\text{ClO}_3^-$  byproduct is treated by either comproportionation under acidic conditions (eq 1) or catalytic reduction by  $H_2$  (eq 2)

Received: May 21, 2020 Revised: June 29, 2020



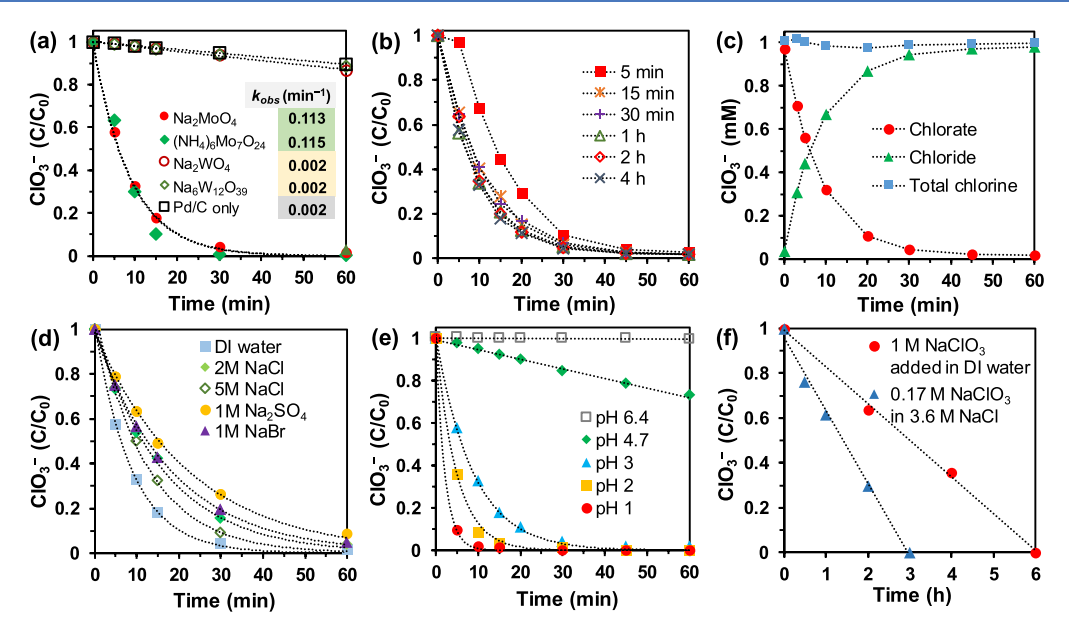


Figure 1. (a) Profiles, first-order fittings, and rate constants for the reduction of  $ClO_3^-$  by Pd/C added with various POM precursors; (b) profiles of  $ClO_3^-$  reduction by the  $MoO_x-Pd/C$  catalyst prepared by allowing variable time lengths after adding the  $Na_2MoO_4$  precursor under 1 atm  $H_2$  and before adding the  $NaClO_3$  substrate; (c) chlorine mass balance; (d) effects of concentrated salts; (e) effects of proton concentrations; and (f) the reduction of 1 M  $ClO_3^-$  in deionized (DI) water and of 170 mM  $ClO_3^-$  in 3.6 M NaCl brine by 0.5 g  $L^{-1}$   $MoO_x-Pd/C$ . Unless specified, all reactions used 1 mM  $ClO_3^-$ , 0.2 g  $L^{-1}$   $MoO_x-Pd/C$ , pH 3.0, 20 °C.

$$ClO_3^- + 6H^+ + 5Cl^- \rightarrow 3H_2O + 3Cl_2$$
 (1)

$$ClO_3^- + 3H_2 \rightarrow Cl^- + 3H_2O$$
 (2)

The comproportionation reaction requires >85 °C and pH 0 (i.e., 1 M of H $^+$ ) to achieve a partial (60–90%) removal of ClO $_3$  $^-$ . The pH adjustment involves large amounts of HCl and NaOH. $^6$  In comparison, catalytic reduction allows an almost complete conversion of ClO $_3$  $^-$  to Cl $^-$  and requires orders of magnitude less acid (i.e., pH 2–4). $^6$  In particular, H $_2$  gas is produced in excess at the cathode of the chlor-alkali process; about 10% of the H $_2$  is emitted to the atmosphere. $^6$  Supported platinum group metal (PGM) catalysts have been examined; however, they exhibit limited activity and require high catalyst loadings to achieve a satisfactory reaction rate.  $^{11,15,16}$  Furthermore, PGM catalysts can be severely inhibited by concentrated salts in the brine.  $^{11,17}$  It is thus highly desirable to develop a ClO $_3$  $^-$  reduction catalyst with the following features: (i) high activity and robustness, (ii) using a relatively abundant metal, and (iii) having a facile preparation.

Polyoxometalates (POMs) of Group 6 Mo and W have a series of fascinating redox properties and have been used in various chemical catalysis. A century ago, molybdate was used as a homogeneous catalyst to reduce  $ClO_3^-$  by  $I^-$  for iodometric analysis. Molybdate was later used in the catalytic polarographic reduction of  $ClO_3^-$  to determine Mo contents in metals. For the reduction of  $ClO_3^-$  in drinking water sources and in brines, an ideal approach is to immobilize Mo species as an active site on solid supports and utilize  $H_2$  as a clean and readily available electron donor. In this study, using a Pd/C catalyst platform and conducting a series of material characterizations, we show that  $Mo^{VI}$  POMs can be transformed into a heterogeneous  $MoO_x$ –Pd/C catalyst, which is highly active and robust for  $ClO_3^-$  reduction under various challenging conditions.

# ■ RESULTS AND DISCUSSION

Catalyst Preparation. We developed a simple and straightforward method to immobilize and activate Mo sites on Pd/C. Inspired by the reductive immobilization of Group 7 metal oxyanions (TcVIIO4- and ReVIIO4-) from aqueous solutions, 21-24 we hypothesized that Group 6 MoVI and WVI POM precursors could be similarly immobilized and reduced to insoluble lower-valent oxide species on Pd/C. Hence, two Mo<sup>VI</sup> POM precursors (nominally 5 wt % as Mo to the weight of Pd/C) were added into the water suspension of Pd/C at room temperature (20  $^{\circ}$ C), with 1 atm H<sub>2</sub> in the headspace of the reactor flask. After 2 h of stirring, 1 mM of NaClO<sub>3</sub> was added into the suspension to probe the catalytic activity. As shown in Figure 1a, the use of Na2MoVIO4 and (NH<sub>4</sub>)<sub>6</sub>Mo<sub>7</sub><sup>VI</sup>O<sub>24</sub> provided rapid ClO<sub>3</sub><sup>-</sup> reduction. The pseudo-first-order rate constants are 55-fold higher than that of the original Pd/C. In comparison, the two WVI POM precursors, Na<sub>2</sub>W<sup>VI</sup>O<sub>4</sub> and Na<sub>6</sub>W<sub>12</sub>V<sup>I</sup>O<sub>39</sub>, provided little activity enhancement.

The immobilization and activation of Mo are both rapid. Inductively coupled plasma-mass spectrometry (ICP-MS) analysis of the aqueous phase found >96% of the initial Mo (10 mg L<sup>-1</sup> as Mo element) adsorbed into Pd/C within 5 min on the benchtop. Without exposure to H<sub>2</sub>, X-ray photoelectron spectroscopy (XPS) characterization observed only Mo<sup>VI</sup> in the Pd/C (see the Characterization of Mo Speciation section). After 1 atm H<sub>2</sub> was supplied to the water suspension of Mo<sup>VI</sup>–Pd/C, high activity of ClO<sub>3</sub><sup>-</sup> reduction was observed. Prior to the addition of NaClO<sub>3</sub>, after Mo<sup>VI</sup>–Pd/C was exposed to H<sub>2</sub> for only 5 min, the profile of ClO<sub>3</sub><sup>-</sup> reduction had an induction period at the beginning (Figure 1b). However, the exposure to H<sub>2</sub> for 15 min or longer eliminated this induction period, providing similar ClO<sub>3</sub><sup>-</sup> reduction kinetics. Thus, the reduction of adsorbed Mo<sup>VI</sup> by Pd-activated H<sub>2</sub> is required to enable ClO<sub>3</sub><sup>-</sup> reduction. This process is rapid, taking only 15 min at ambient pressure and temperature. Detailed

Table 1. Performance of ClO<sub>3</sub><sup>-</sup> Reduction by MoO<sub>x</sub>-Pd/C and Reported PGM Catalysts

entry	catalyst	catalyst loading	hЧ	temp	initial ClO <sub>3</sub> <sup>-</sup> concentration	other salts added in solution	time	ClO <sub>3</sub> <sup>-</sup> removal ratio	$1^{st}$ -order rate constant <sup>a</sup> (L h <sup>-1</sup> g <sub>cat</sub> <sup>-1</sup> )	ref
					$MoO_x-Pd/C$ Catalyst	atalyst				
П	(5 wt % Mo 5 wt % Pd) $MoO_x-Pd/C$	$0.2~{ m g~L^{-1}}$	ъ	20 °C	84 mg L <sup>-1</sup> (1 mM)	$\mathrm{DI}_{p}$	1 h	%6.66	33.9	
7						2 M NaCl	1 h	%26	18.3	
3						5 M NaCl	1 h	%6.66	24.6	
4						1 M NaBr	1 h	%56	16.5	
S						$1 \text{ M Na}_2 \text{SO}_4$	1 h	91%	13.5	
9	(5 wt % Mo 5 wt % Pd) $MoO_x-Pd/C$	$0.5~\mathrm{g~L^{-1}}$	3	20 °C	$84\ 000\ \mathrm{mg\ L^{-1}}\ (1\ \mathrm{M})$	DI, KCl built up to 1 M	6 h	%2.66	$0.33 \text{ mol h}^{-1} \text{ g}_{\text{cat}}^{-1c}$	
7					$14 280 \text{ mg L}^{-1} (0.17 \text{ M})$	3.6 M NaCl	3 h	%8'66	$0.11 \text{ mol h}^{-1} \text{ g}_{\text{cat}}^{-1c}$	
					PGM Catalysts	sts				
∞	S wt % Pd/C	$0.5~\mathrm{g~L^{-1}}$	33	20 °C	84 mg L <sup>-1</sup> (1 mM)	DI	8 h	%96	0.79	17
6						10 mM NaCl	8 h	81%	0.41	17
10						100 mM NaCl	8 h	49%	0.17	17
11						1 M NaCl	8 h	43%	0.14	17
12						10 mM NaBr	8 h	42%	0.13	17
13	5 wt % Rh/C	$0.5~\mathrm{g~L^{-1}}$	ъ	20 °C	84 mg L <sup>-1</sup> (1 mM)	DI	1/4 h	99.3%	46	15
14	5 wt % Ru/C						1 h	43%	na <sup>d</sup>	15
15	5 wt % Pt/C						1 h	14%	0.33	15
16	1 wt % Ir/C						1 h	45%	1.2	15
17	5 wt % Ir/C	$2.5 \text{ g L}^{-1}$	3.8	20° C	$22\ 000\ \mathrm{mg\ L^{-1}}\ (0.26\ \mathrm{M})$	3.2 M NaCl	3/4 h	100%	$0.14 \text{ mol h}^{-1} \text{ g}_{\text{cat}}^{-1}$	16
18	0.5 wt % Rh/SiC	$0.5~\mathrm{g~L^{-1}}$	4	20° €	1000 mg L <sup>-1</sup> (12 mM)	DI	2 h	85%	$1.9^e$	11
19	0.5 wt % Pt/SiC						2 h	%06	2.3	11
20	0.5 wt % Rh/SiC	$0.5~\mathrm{g~L^{-1}}$	2	S0 °C	1000 mg L <sup>-1</sup> (12 mM)	DI	2 h	35%	0.43	11
21						3.6 M NaCl	2 h	10%	0.11	11
22	$0.5 \text{ wt} \% \text{ Rh/ZrO}_2$	$2~{ m g~L^{-1}}$	4	20° C	$1000 \text{ mg L}^{-1} (12 \text{ mM})$	DI	2 h	%68	0.55	11
23						0.85 M NaCl	2 h	45%	0.15	11
24						78 mM NaBr	2 h	27%	0.079	11

<sup>a</sup>Normalized to the mass of the whole catalyst (metal + support) for cross-comparison of catalysts with variable metal contents. <sup>b</sup>Containing HCl or H<sub>2</sub>SO<sub>4</sub> used for pH adjustment. <sup>c</sup>Zero-order kinetics due to the concentrated ClO<sub>3</sub> substrate; these two reactions used the same high flow rate of H<sub>2</sub> (0.1 L per minute) as used for entries 18–24. <sup>a</sup>The reaction did not follow first- or zero-order kinetics and the catalyst showed significant loss of activity during the reaction. First-order rate law reasonably assumed for the initial CIO<sub>3</sub> concentration at 12 mM (entries 18-24).

characterizations of the lower-valent Mo species are provided in the later sections.

Upon H<sub>2</sub> exposure for 2 h, the Mo immobilization ratio was further increased to 99.9% (Figure S1). Throughout the ClO<sub>3</sub> reduction process, <15  $\mu$ g L<sup>-1</sup> of Mo (i.e., <0.15% of the total added Mo) was detected by ICP-MS in the aqueous solution. Thus, the carbon support of Pd/C has a high capacity to accommodate MoO<sub>x</sub> species. It also appears that ClO<sub>3</sub><sup>-</sup> reduction occurred on the heterogeneous catalyst-water interface. In contrast, the same Pd/C material provided a poor sorption capacity for WO<sub>x</sub> species. ICP-MS analysis showed that only 24% of the added W was immobilized after exposure to H<sub>2</sub> for 2 h. The reduced W species in the aqueous solution showed a blue color, which faded within 1 min after exposure to air. Therefore, the reductive immobilization method applies to MoVI POMs to yield a highly active MoO<sub>x</sub>-Pd/C catalyst. In aqueous solutions, Mo<sup>VI</sup> POMs have dynamic speciations depending on pH. Both Na<sub>2</sub>MoO<sub>4</sub> and (NH<sub>4</sub>)<sub>6</sub>Mo<sub>7</sub>O<sub>24</sub> added in an acidic solution (e.g., pH 3) transform into a mixture of Mo<sub>8</sub>O<sub>26</sub><sup>4-</sup>, H<sub>3</sub>Mo<sub>8</sub>O<sub>28</sub><sup>5-</sup>,  $\text{HMo}_7\text{O}_{24}^{5-}$ ,  $\text{H}_2\text{Mo}_6\text{O}_{21}^{4-}$ , and other minor polymeric species. 25 To avoid introducing the unnecessary NH<sub>4</sub>+, we used Na<sub>2</sub>MoO<sub>4</sub> as the Mo precursor for the following experiments.

Catalyst Performance. The MoO<sub>x</sub>-Pd/C catalyst outperforms multiple reported PGM catalysts in terms of the activity for ClO<sub>3</sub><sup>-</sup> reduction and the robustness in concentrated brines. At 20 °C, a loading of 0.2 g L<sup>-1</sup> catalyst in water achieved >99.9% reduction of 1 mM ClO<sub>3</sub><sup>-</sup> within 1 h (Figure 1a). The observed rate constant is substantially higher than those of most PGM catalysts at the same or higher temperatures (Table 1). Calculation suggests that the rate of ClO<sub>3</sub><sup>-</sup> reduction is not limited by either internal or external mass transfer of aqueous ClO<sub>3</sub><sup>-</sup> with regard to the catalyst particle (see the Supporting Information). The mass balance between ClO<sub>3</sub><sup>-</sup> and Cl<sup>-</sup> throughout the reaction (Figure 1c) indicates minimal accumulation of partially deoxygenated intermediates (e.g., ClO<sub>2</sub><sup>-</sup>). In real-world situations, ClO<sub>3</sub><sup>-</sup> needs to be reduced in acidic and/or brine matrices, such as chlor-alkali waste brines, 10,16 ion-exchange resin regeneration wastes, <sup>26</sup> or HCl produced from waste brine electrolysis. <sup>14</sup> Therefore, we further challenged the performance of MoO<sub>x</sub>-Pd/C in solutions containing 2 M and 5 M NaCl, 1 M Na<sub>2</sub>SO<sub>4</sub>, and 1 M NaBr, respectively. None of the concentrated salts caused a significant loss of activity (Figure 1d and Table 1, entries 1–5). We note that Br<sup>-</sup> is a much stronger inhibitor than Cl<sup>-</sup> for PGM catalysts. 11,17 The same Pd/C was significantly inhibited by halide anions at low concentrations, as observed in our previous study (Table 1, entries 8–12).<sup>17</sup> Similarly, although a Rh/C catalyst exhibited very high activity in a deionized water matrix (Table 1, entry 13), 15 the performance was significantly affected by Cl<sup>-</sup> and Br<sup>-</sup> (Table 1, entries 20–24). An Ir/C catalyst showed similar ClO<sub>3</sub> reduction kinetics to the MoO<sub>x</sub>-Pd/C in concentrated brine (Table 1, entry 17 versus 7), whereas the reaction temperature was much higher (70 °C). 16

Higher rates of ClO<sub>3</sub><sup>-</sup> reduction were observed at lower pH conditions (Figure 1e), suggesting that a proton-assisted mechanism is involved. We note that the pH dependence may be primarily attributed to the reactivity of the active site rather than the surface charge of the catalyst support. <sup>15,27</sup> Instead, the protonation of an O atom in the ClO<sub>3</sub><sup>-</sup> that is bound by the lower-valent Mo may assist the structural

distortion.<sup>28</sup> This structural change lowers the LUMO of Mobound ClO<sub>3</sub><sup>-</sup> and thus promotes the electron transfer from reduced Mo (e.g., Mo<sup>IV</sup>) to Cl<sup>V</sup>. Alternatively, the proton may provide an ancillary hydrogen bonding<sup>29</sup> to facilitate the coordination of ClO<sub>3</sub><sup>-</sup> to Mo. Thus, the MoO<sub>x</sub>-Pd/C catalyst is expected to be highly robust in reducing ClO<sub>3</sub><sup>-</sup> in acidic brines. <sup>14</sup> Because the build-up of Cl<sup>-</sup> did not cause a significant inhibition, we further tested the catalyst for treating concentrated ClO<sub>3</sub><sup>-</sup> (1 M) at pH 3.0. With a 0.5 g L<sup>-1</sup> loading of the MoO<sub>x</sub>-Pd/C catalyst, >99.7% reduction of ClO<sub>3</sub> was achieved within 6 h following zero-order kinetics (Figure 1f). When ClO<sub>3</sub><sup>-</sup> concentrations were high, the reaction rate became controlled by the H2 availability (Figure S2). Assuming that the Mo sites reacted with all  $ClO_x^-$  (x = 3, 2, and 1) substrates, at pH 3 the corresponding TON for each Mo atom is calculated as 11,510 within 6 h (i.e., turnover frequency  $TOF = 1920 \text{ h}^{-1}$ ). If not all immobilized Mo atoms were directly involved in the reaction (see the catalyst characterization results below), the actual TOF on the reactive Mo sites would be even higher. As shown in Figure 1e, a higher TOF can also be expected at pH < 3.

We prepared a solution mimicking a real chlor-alkali waste brine sample (0.17 M of  ${\rm ClO_3}^-$  in 3.6 M of NaCl). <sup>11</sup> The  ${\rm MoO_x-Pd/C}$  catalyst achieved >99.8% reduction of  ${\rm ClO_3}^-$  in 3 h (Figure 1f and Table 1, entry 7). To further examine the catalyst stability and reusability, we added multiple spikes of 180 mM  ${\rm ClO_3}^-$ , for up to 20 spikes (the final product thus became 3.6 M NaCl), into the catalyst suspension in water (Figure S3, zero-order rate constants shown in Table 2). Each spike of  ${\rm ClO_3}^-$  was completely reduced within 4 h. The decrease of the catalytic activity was only caused by the gradual build-up of concentrated  ${\rm Cl}^-$ . In particular, the reduction profile for the  $20^{\rm th}$  NaClO<sub>3</sub> spike corresponds to a zero-order rate constant of 0.13 mol h<sup>-1</sup>  ${\rm g_{cat}}^{-1}$ . This rate constant, after the catalyst had been used to reduce 19 spikes of 0.18 M

Table 2. Kinetics and Metal Contents of the Freshly Prepared and Used MoO<sub>x</sub>-Pd/C Catalysts<sup>a</sup>

catalyst sample	Mo content	Pd content	Mo wt %: Pd wt % <sup>b</sup>	zero-order initial rate constant <sup>c</sup> (mol $h^{-1} g_{cat}^{-1}$ )
fresh catalyst	4.48%	5.73%	0.782	0.271 (in DI water)
after 5 spikes	4.38%	5.51%	0.795	0.186 (in 0.9 M NaCl) <sup>d</sup>
after 10 spikes	4.19%	5.61%	0.747	0.141 (in 1.8 M NaCl) <sup>d</sup>
after 20 spikes	4.39%	5.70%	0.771	0.130 (in 3.6 M NaCl) <sup>d</sup>
	fresh catalyst after 5 spikes after 10 spikes after 20	sample content fresh 4.48% catalyst after 5 4.38% spikes after 10 4.19% spikes after 20 4.39%	sample         content         content           fresh catalyst         4.48%         5.73%           after 5 spikes         4.38%         5.51%           after 10 spikes         4.19%         5.61%           after 20         4.39%         5.70%	sample         content         content         Mo wt %: Pd wt %b           fresh catalyst         4.48%         5.73%         0.782           after 5 spikes         4.38%         5.51%         0.795           after 10 spikes         4.19%         5.61%         0.747           after 20         4.39%         5.70%         0.771

"The nominal content for Mo and Pd elements in the freshly prepared catalyst are both 5 wt %. The calculated Mo content assuming the addition of "MoO<sub>4</sub>" in Pd/C is  $\sim$ 4.62%. Each spike introduced 180 mM ClO<sub>3</sub><sup>-</sup>. At least 4 h of reaction (1 atm H<sub>2</sub>, 20 °C, initial pH = 3 by adding 1 mM HCl) was allowed for each spike. The catalyst powder was collected in an anaerobic glove bag by filtering off the aqueous solution, rinsing the catalyst powder cake on the filter paper with DI water, and drying in a 100 °C sand bath. <sup>b</sup>Because the Mo/Pd mass content ratios are rather consistent, the fluctuation of the absolute values of Mo and Pd contents in these samples should either be within the range of system errors of elemental analysis for heterogeneous materials or be attributed to the residual NaCl salt in the dried catalyst samples. <sup>c</sup>From the linear fitting of all data points with  $C/C_0 > 0.2$  (see Figure S3b for details). <sup>d</sup>The NaCl is generated from the reduction of ClO<sub>3</sub><sup>-</sup> from all previous spikes (180 mM each).

Table 3. Physisorption and Chemisorption Data

sample	surface Area $(m^2 g_{cat}^{-1})$	pore volume $(cm^3 g_{cat}^{-1})$	average pore size (nm)	Pd surface area $(m^2 g_{cat}^{-1})$	Pd dispersion (%)	Pd particle size (nm)
Pd/C	857.2	0.67	3.11	6.85	30.7	3.7
MoOPd/C	689.0	0.54	3.12	2.29	N/A <sup>a</sup>	N/A <sup>a</sup>

<sup>&</sup>quot;The calculated Pd dispersion and average particle size are 10.3% and 10.8 nm, respectively. This set of data is not meaningful as it is calculated from the reduced Pd surface area by the immobilized MoO<sub>v</sub>.

Table 4. Mo K-Edge EXAFS Shell-by-Shell Fitting Parameters of MoO<sub>x</sub>-Pd/C and References

sample	shell	CN <sup>a</sup>	$R (Å)^b$	$\sigma^2 (\mathring{A}^2)^c$	$\Delta E (eV)^d$	R-factor
$(NH_4)_6Mo_7O_{24}$	Mo-O	4	1.74 (0.01)	0.004 (0.002)	-4.0 (3.3)	0.012
$MoO_2$	Mo-O	6	1.99 (0.01)	0.002 (0.001)	-1.4(2.0)	0.023
	Mo-Mo	1	2.52 (0.01)	0.001 (0.001)		
	Mo-Mo	1	3.12 (0.01)	0.002 (0.001)		
	Mo-Mo	8	3.70 (0.01)	0.004 (0.001)		
$MoO_x-Pd/C$	Mo-O	0.4 (0.3)	1.67 (0.04)	$0.002^{e}$	-4.1(2.9)	0.030
	Mo-O	6.1 (1.9)	2.03 (0.02)	0.010 (0.004)		
	Mo-Mo	1.7 (0.6)	2.56 (0.01)	0.005 (0.002)		

<sup>&</sup>lt;sup>a</sup>Coordination number (CN). <sup>b</sup>Interatomic distance. <sup>c</sup>Debye—Waller factor. <sup>d</sup>Energy shifts. During the EXAFS shell-by-shell fitting for the two references, the CNs were fixed at theoretical values according to their crystal structures. <sup>e</sup>Fixed during the fitting.

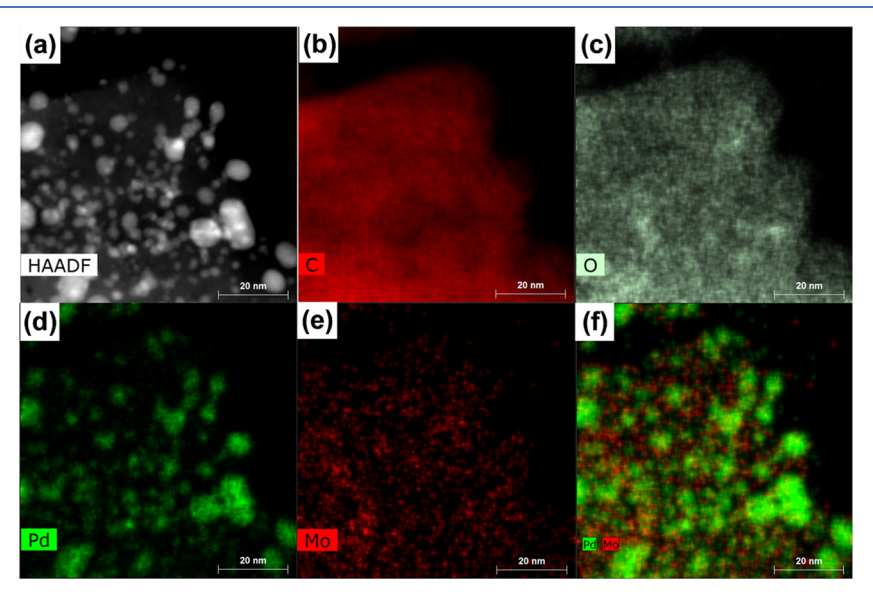


Figure 2. (a) HAADF-STEM imaging of the  $MoO_x$ -Pd/C catalyst and EDX mapping of (b) C, (c) O, (d) Pd, and (e) Mo. (f) Combined Pd and Mo mapping showing the different distribution of the two elements.

ClO<sub>3</sub><sup>-</sup> in the gradually concentrated NaCl, is almost identical to that of the freshly prepared catalyst (Table 1, entry 7). The reduction of ClO<sub>3</sub><sup>-</sup> did not consume H<sup>+</sup>, so that the initially added 1 mM H<sup>+</sup> (for pH 3.0) maintained the acidic pH throughout the 20 spikes. The final pH reading was ~2.5 because the resulted 3.6 M NaCl decreased the hydration of H<sup>+</sup>.<sup>30</sup> The Mo and Pd contents in the catalysts collected after 5, 10, and 20 spikes remained consistent (Table 2), indicating negligible leaching of metals into the high-salinity aqueous solutions. A catalyst recycling operation using the conventional "filtration-collection-redispersion" procedure resulted in a slightly decreased performance (Figure S4a), most probably due to the loss of a nonrecoverable fraction of catalyst during the sample transfer (e.g., held by the filter paper). The filtrate solution contained <0.1% of total Mo. Therefore, the reductively immobilized MoO<sub>x</sub> species in Pd/C showed high activity, robustness, and stability for catalytic ClO<sub>3</sub><sup>-</sup> reduction.

Characterization of Mo Speciation. The immobilization of Mo POMs in Pd/C decreased both the Brunauer-Emmett-Teller (BET) surface area and the Pd surface area (Table 3). For a rough estimation of  $MoO_x$  coverage on the carbon support, one could assume that each MoO, unit is six coordinate and takes a square area at the length of an O-Mo-O. Since the atomic radius of O atom is ~60 pm and the typical Mo-O bond length is ~200 pm (see extended X-ray absorption fine structure (EXAFS) analysis and Table 4), the corresponding length of an O-Mo-O is  $(60 + 200) \times 2 = 520$ pm. Thus, a single layer of MoO<sub>x</sub> at the 5 wt % Mo loading in one gram of carbon support is calculated to be 86 m<sup>2</sup>. The carbon support has a sufficient surface area to accommodate a single-layer coverage of MoO<sub>x</sub>. The decrease in pore volume (19.4%) was very similar to the decrease in surface area (19.6%), indicating that the loss of BET surface area is probably attributed to both the pore blocking and surface covering by the immobilized MoO<sub>x</sub>. High-angle annular dark-

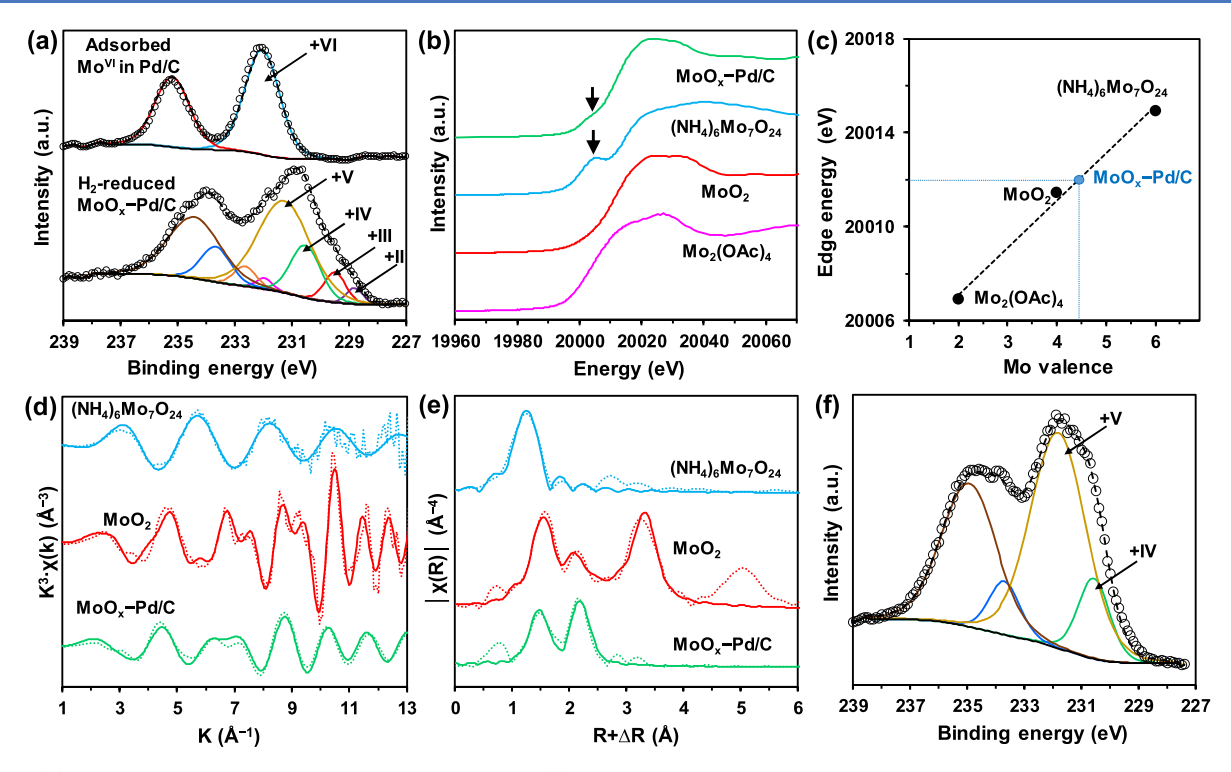


Figure 3. (a) Mo 3d XPS spectra of the  $MoO_x-Pd/C$  samples; (b) Mo K-edge XANES spectra of the reduced  $MoO_x-Pd/C$  and references, with the two arrows indicating the characteristic pre-edge peak for oxo- $Mo^{VI}$  species; (c) the correlation between Mo K-edge energies and valences for the references; (d) Mo K-edge EXAFS spectra of the reduced  $MoO_x-Pd/C$  and references and their shell-by-shell fits; (e) the EXAFS Fourier transforms and their fits, and (f) Mo 3d XPS spectrum of the solid residue from the dried aqueous solution of  $Na_2MoO_4$  after the reduction using hydrazine. In the XPS and EXAFS spectra (panels a, d, e, and f), the dotted and solid lines represent spectra and their fits, respectively.

field scanning transmission electron microscopy (HAADF-STEM) characterization of the  $MoO_x$ -Pd/C catalyst observed Pd nanoparticles in the size of 1–8 nm (Figure 2a). Individual elements of C, O, Pd, and Mo were observed by the energy-dispersive X-ray (EDX) elemental mapping (Figure 2b–e). Mo was present throughout the catalyst particle, either being on the carbon support or overlapping with Pd (Figure 2f).

XPS characterization of the H<sub>2</sub>-reduced MoO<sub>x</sub>-Pd/C catalyst (kept under an anaerobic atmosphere) identified Pd<sup>0</sup>, which showed the characteristic 3d<sub>5/2</sub> binding energy (BE) at 335.2 eV (Figure S5a) and various oxidation states of Mo (Figure 3a). Because the  $MoO_x$ -Pd/C catalyst and the references such as Mo<sub>2</sub><sup>II</sup>(OAc)<sub>4</sub> contain different carbon species (i.e., graphitic carbon versus acetate), we blended Nb<sub>2</sub>O<sub>5</sub> powders with all XPS samples as the internal standard for BE calibration (Figure S5b, Nb  $3d_{5/2}$  BE set to 207.6 eV<sup>31</sup>). Upon deconvoluting the spectrum for MoO<sub>x</sub>-Pd/C, we identified four Mo doublets with 3d<sub>5/2</sub> BE of 231.3, 230.5, 229.4, and 228.7 eV. The two dominant  $3d_{5/2}$  peaks with BE of 231.3 and 230.5 eV closely match literature values for Mo<sup>V</sup> and Mo<sup>IV</sup> species. The Mo<sup>V</sup> reference was generated from a hydrothermal synthesis of a Keggin POM from  $Na_2Mo^{VI}O_4^{\ 32,33}$  and the  $Mo^{IV}$  reference was generated from a direct reduction of Mo<sup>VI</sup>O<sub>3</sub> by H<sub>2</sub> at 400 °C.<sup>34</sup> The observed  $Mo^{V}$  and  $Mo^{IV}$  in the  $MoO_x$ -Pd/C should be generated by the partial and full hydrogenation of one oxo bond in Mo<sup>VI</sup> POM precursors.<sup>34</sup> Due to the wide range of BE values for Mo species in lower oxidation states, Mo<sub>2</sub><sup>II</sup>(OAc)<sub>4</sub> was used as a reference. The XPS spectrum revealed two Mo oxidation states on the surface of Mo<sub>2</sub><sup>II</sup>(OAc)<sub>4</sub> (Figure S5c). The high BE peak (232.3 eV) is characteristic of MoVI, indicating partial oxidation at the surface of Mo<sub>2</sub><sup>II</sup>(OAc)<sub>4</sub> powders. The 3d<sub>5/2</sub>

BE of  $Mo^{II}$  is 228.9 eV, which is close to the lowest BE (228.7 eV) observed in  $MoO_x$ –Pd/C. The remaining peak (BE 229.4 eV) in the catalyst is thus assigned as  $Mo^{III}$ , although a reference chemical for oxygen-coordinated  $Mo^{III}$  was not accessible. Compared to the formation of  $Mo^{V}$  and  $Mo^{IV}$  from  $Mo^{VI}$ , the formation of the less abundant  $Mo^{III}$  and  $Mo^{II}$  can be attributed to the deeper but less favorable reduction of  $Mo^{IV}$ . Without exposure to  $H_2$ , the oxidation state of the adsorbed  $Mo^{VI}$  POMs in Pd/C remained the same (Mo  $3d_{5/2}$  BE at 232.0 eV, Figure 3a).

To further probe the valence of Mo species in the bulk MoO<sub>x</sub>-Pd/C sample, we conducted Mo K-edge X-ray absorption near-edge structure (XANES) spectroscopic characterization (Figure 3b). A linear relationship<sup>35</sup> was established between the Mo oxidation state and the Mo Kedge energy (i.e., the energy where the intensity reaches 60% of the absorption maxima) of three references:  $(NH_4)_6Mo_7^{VI}O_{24}$ ,  $Mo^{IV}O_2$ , and  $Mo_2^{II}(OAc)_4$  (Figure 3c). With this empirical relationship and the measured edge energy of 20012 eV for MoO<sub>x</sub>-Pd/C, the average valence of Mo in the bulk sample is calculated to be 4.4. This value roughly agrees with the XPS characterization result for the surface layer, where Mo<sup>IV</sup> and Mo<sup>V</sup> are dominant species. Moreover, the XANES spectrum of (NH<sub>4</sub>)<sub>6</sub>Mo<sub>7</sub><sup>VI</sup>O<sub>24</sub> contains a pre-edge peak at 20003 eV. The presence and absence of this characteristic pre-edge peak indicate the formation and elimination of Mo<sup>VI</sup>=O bonds, respectively. 35,36 The significantly weakened pre-edge peak in MoO,-Pd/C (Figure 3b) indicates the reduction of Mo=O bonds in MoVI POM precursors.

To determine whether the reductively immobilized Mo species exist as oxide clusters or as monomers (e.g., stabilized

by complexation with functional groups on the carbon surface), we collected the  $k^3$ -weighted Mo K-edge extended X-ray absorption fine structure (EXAFS) spectra from the  $MoO_x-Pd/C$  sample and references (Figure 3d,e). The MoO<sub>x</sub>-Pd/C spectrum contained two main peaks at 1.5 and 2.2 Å  $(R + \Delta R)$ . Shell-by-shell fitting (Table 4) showed that they correspond to two atomic shells, Mo<sup>IV</sup>-O (2.03 Å) and Mo<sup>IV</sup>-Mo<sup>IV</sup> (2.56 Å).<sup>37</sup> Similar EXAFS spectra have been reported in a study on the complete and reversible 24-electron reduction of a well-defined solid-state  $[PMo_{12}^{VI}O_{40}]^{3-}$  into  $[PMo_{12}^{IV}O_{40}]^{27-}$  on a battery reaction platform, 35 where the Mo–Mo distance was shortened from 3.4 to 2.6 Å upon the reduction of all Mo<sup>VI</sup> into Mo<sup>IV</sup>. Since Mo<sup>VI</sup> precursors were transformed into a mixture of multiple POM structures in the aqueous solution and XPS characterization observed mixed oxidation states of Mo at the surface layer, the EXAFS fitting here represents the average bonding environment for the bulk  $MoO_x$ -Pd/C sample. The average coordination number (CN) of 6.1 for the Mo-O shell indicates that a majority of reduced Mo atoms are in the octahedral MoO<sub>6</sub> coordination structure. The overall CN of 1.7 for Mo-Mo shell confirms the polymeric structures for reductively immobilized Mo species. A majority of Mo atoms likely have two neighboring Mo atoms at a distance of ~2.56 Å. Furthermore, the lack of Mo-Mo pairs with longer interatomic distances as observed in Mo<sup>IV</sup>O<sub>2</sub> reference (>3 Å, Figure 3e and Table 4) suggests that the spatial arrangement of Mo atoms in MoO<sub>x</sub>-Pd/C is different from that in Mo<sup>IV</sup>O<sub>2</sub>. The latter has a three-dimensional distorted rutile structure with alternating short (2.51 Å) and long (3.11 Å) Mo<sup>IV</sup>–Mo<sup>IV</sup> distances.<sup>37</sup> The fitting also detects a weak atomic shell at 1.67 Å, which can be assigned to the Mo<sup>VI</sup>=O bond as observed in (NH<sub>4</sub>)<sub>6</sub>Mo<sub>7</sub><sup>VI</sup>O<sub>24</sub> reference (1.74 Å, Table 4). Thus, a small fraction of immobilized Mo remained in +VI valence, but it was not observed by XPS characterization on the catalyst surface. The inclusion of a Mo-Pd shell yielded problematic data fitting (Table S1), suggesting that the direct bonding between the two metals is not a primary mechanism for the immobilization and activation of Mo. However, chemisorption results show that the immobilization of MoO<sub>x</sub> decreased the total surface area and the Pd surface area by  $^{1}168~m^{2}~g^{-1}~(20\%)$  and  $4.6~m^{2}~g^{-1}$ (66%), respectively (Table 3). The higher percent decrease in the Pd surface area suggests a preferred aggregation of MoO<sub>x</sub> in the proximity of Pd nanoparticles.3

Mechanistic Insights. Since a negligible fraction of Mo was detected in aqueous phase throughout the reduction of ClO<sub>3</sub><sup>-</sup>, it appears that the catalytic site is surface-immobilized and that the reduction of MoO<sub>x</sub> species by H<sub>2</sub> occurs on the carbon support. To further rule out the possibility that the reactive site is dissolved Mo in aqueous solution, we conducted control reactions without involving Pd/C or H<sub>2</sub> in the gaswater-solid three-phase system. In the first experiment, the use of Na<sub>2</sub>Mo<sup>VI</sup>O<sub>4</sub> and H<sub>2</sub> (without Pd/C) did not reduce ClO<sub>3</sub> (Figure S4b), indicating the critical role of Pd nanoparticles in harvesting electrons from H2. In another experiment, the Na<sub>2</sub>Mo<sup>VI</sup>O<sub>4</sub> solution was heated with 6.5 equivalents of hydrazine at pH 3 and 70 °C. This system has been reported to reduce Mo<sup>VI</sup> in the aqueous phase.<sup>39</sup> XPS characterization of the residue (slowly dried at 70 °C under anaerobic conditions) observed two Mo 3d<sub>5/2</sub> peaks at 231.5 and 230.4 eV (Figure 3f), which can be readily assigned as Mo<sup>V</sup> and Mo<sup>IV</sup>, respectively. However, the aqueous solution containing both reduced Mo species and excess hydrazine did

not show any  ${\rm ClO_3}^-$  reduction activity, even after 24 h of heating at 70 °C. Therefore, a homogeneous reduction of  ${\rm ClO_3}^-$  by the reduced Mo species from  ${\rm Na_2Mo^{VI}O_4}$  is unlikely. The structural and reactivity differences of the reduced Mo species in solution and on carbon support warrant further investigation. Nonetheless, all kinetic and characterization results collectively confirm the heterogeneous nature of the  ${\rm MoO_x-Pd/C}$  catalyst. Furthermore, the change of reaction kinetics from first order at low  ${\rm ClO_3}^-$  concentrations to zero order at high  ${\rm ClO_3}^-$  concentrations (Figures 1 and S3a) can be readily explained by the Langmuir—Hinshelwood mechanism describing heterogeneous catalysis.

For the catalytic reduction of  $ClO_3^-$ , we propose that the surface-immobilized  $MoO_x$  species and Pd nanoparticles play separate roles (i.e., oxygen atom transfer (OAT) with  $ClO_x^-$  by Mo and activation of  $H_2$  by Pd, respectively), rather than POM enhancing the activity of Pd nanoparticles. The original Pd/C has high activity in the reduction of bromate (BrO $_3^-$ ) but no activity in the reduction of nitrate (NO $_3^-$ ). The immobilization of MoO $_x$  neither increased the BrO $_3^-$  reduction activity (Figure S6a) nor enabled NO $_3^-$  reduction (Figure S6b). Thus, the addition of MoO $_x$  in Pd/C did not increase the "intrinsic" activity of Pd nanoparticles. Instead, the results with BrO $_3^-$  and NO $_3^-$  suggest the unique selectivity of reduced Mo species towards  $ClO_3^-$ .

Based on the spectroscopic findings, we propose a representative catalytic cycle in Scheme 1. The Mo<sup>VI</sup> POM precursor (multiacid form 1, in equilibrium with the oxo-Mo<sup>VI</sup> structure 1') is immobilized onto the carbon support and

Scheme 1. Proposed Reaction Mechanism and a Model Local Structure of Mo<sup>IV</sup> Species 3 Based on EXAFS Analysis

undergoes the reduction of Mo<sup>VI</sup>=O to Mo<sup>V</sup>-OH (2). The electron comes from Pd-activated H2. A further one-electron reduction generates Mo<sup>IV</sup>-OH<sub>2</sub> (3). A similar reduction of a 10 nm layer of Mo<sup>VI</sup>O<sub>3</sub> by H<sub>2</sub> at room temperature to yield Mo<sup>V</sup> and Mo<sup>IV</sup> species and H<sub>2</sub>O on a Pd membrane has been reported.<sup>41</sup> The dissociation of H<sub>2</sub>O from 3 allows the coordination between the Mo<sup>IV</sup> center and a ClO<sub>3</sub><sup>-</sup> (4), followed by a two-electron OAT reaction, resulting in the formation of  $Mo^{VI}$ =O and the dissociation of  $ClO_2^-$ . An  $H^+$  is necessary to facilitate OAT from Cl to Mo. The daughter products ClO<sub>2</sub><sup>-</sup> and ClO<sup>-</sup> have much higher reactivity than ClO<sub>3</sub>-.42 Although Pd nanoparticles can also rapidly reduce the daughter products, the more favorable site should still be the reduced Mo because a major fraction of Pd nanoparticles has been "blocked" by MoO<sub>x</sub> (Table 3). Therefore, a complete reduction of ClO<sub>3</sub><sup>-</sup> into Cl<sup>-</sup> involves up to three OAT redox cycles of Mo. We highlight that the reaction with ClO<sub>x</sub><sup>-</sup> should involve the transfer of an oxygen atom to the Mo cluster. Thus, this process is different from the direct electron transfer with the solid-state [PMo<sub>12</sub>O<sub>40</sub>]<sup>x-</sup> structure, which only alters the bond distance within the intact Keggin cluster.<sup>35</sup> Since the average Mo valence in the H<sub>2</sub>-reduced bulk MoO<sub>x</sub>-Pd/C is 4.4, we propose that the primary catalytic mechanism is the Mo<sup>VI</sup>/Mo<sup>IV</sup> redox cycling. This Mo redox pair for OAT has been confirmed by bioinorganic chemistry studies, 43 including the reduction of nitrate with biomimetic Mo complexes.<sup>4</sup> Other redox cycles such as Mo<sup>IV</sup>/Mo<sup>II</sup> and Mo<sup>V</sup>/Mo<sup>III</sup> may have also contributed to the reactions. The Mo<sup>IV</sup>/Mo<sup>II</sup> cycle has been employed for OAT from CO<sub>2</sub> and N<sub>2</sub>O. 45 The Mo<sup>V</sup>/ Mo<sup>III</sup> cycle has been observed for OAT from sulfoxide to phosphine.<sup>46</sup> However, a direct reaction between oxyanions and Mo<sup>II</sup> or Mo<sup>III</sup> has not been confirmed and warrants further studies. At the water-catalyst heterogeneous interface, the highly oxophilic reduced Mo species can be readily generated from Mo<sup>VI</sup> POMs by Pd-catalyzed hydrogenation under ambient temperature and pressure. The Mo sites exhibit excellent binding affinity and unprecedentedly high reactivity with ClO<sub>3</sub><sup>-</sup>. Common anions such as Cl<sup>-</sup>, Br<sup>-</sup>, and SO<sub>4</sub><sup>2-</sup> in 3 orders-of-magnitude higher concentrations do not have significant inhibition on the catalytic activity. The significantly decreased surface area of Pd after Mo immobilization (Table 3) suggests the probable coverage of Pd nanoparticles by MoO<sub>x</sub> species. Such coverage is assumed to protect Pd from halide poisoning but does not block the diffusion of H<sub>2</sub>.<sup>41</sup>

The findings further contribute to the understanding of the redox transformation of MoVI POMs added to PGM hydrogenation catalysts. In a recent study on catalytic cyclohexane oxidation with an  $O_2-H_2$  mixture,  $^{47}$  the  $PMo_{12}{}^{VI}O_{40}{}^{3-}$  added into a Pt/C suspension in acetonitrile became partially adsorbed. Under the O2-H2 atmosphere at 35 °C, up to four of the twelve MoVI atoms were reduced to Mo<sup>V</sup>, forming PMo<sub>8</sub><sup>VI</sup>Mo<sub>4</sub><sup>V</sup>O<sub>40</sub><sup>7-</sup>. The Pt-activated O<sub>2</sub> and two equivalents of H<sup>+</sup> were transferred to the Mo<sup>V</sup> sites and yielded Mo<sup>V</sup>-bound H<sub>2</sub>O<sub>2</sub>, which further oxidized cyclohexane. Hence, in both bimetallic systems (i.e., PMo<sub>12</sub>-Pt/C and MoO<sub>x</sub>-Pd/ C), the Pt or Pd nanoparticles play the role of activating the dissolved and adsorbed gases ( $O_2$  and/or  $H_2$ ), and the reduced POMs act as the oxophilic site (for Mo-bound peroxide or ClO<sub>x</sub><sup>-</sup>) to enable further steps. Furthermore, the nearcomplete immobilization and deep reduction of the Na<sub>2</sub>Mo<sup>VI</sup>O<sub>4</sub> precursor in this study suggest the influence of specific POM structures and solvents on the extent of adsorption onto support materials and of valence change upon hydrogenation.

#### CONCLUSIONS

The incorporation of an abundant MoVI precursor, NaMoO4, in Pd/C yields a highly active and robust catalyst for the complete reduction of aqueous ClO<sub>3</sub><sup>-</sup> into Cl<sup>-</sup> by 1 atm H<sub>2</sub> under ambient temperature. The Na<sub>2</sub>Mo<sup>VI</sup>O<sub>4</sub> precursor is rapidly adsorbed from the aqueous solution onto the carbon support and reduced by Pd-activated hydrogen into a mixture of low-valent Mo oxide species. The primary mechanism for chlorate reduction is proposed to be the OAT from ClO, substrates to the surface-immobilized Mo<sup>IV</sup> species. The Mo sites also show a high selectivity toward ClO<sub>3</sub><sup>-</sup> over other oxyanions. The high activity and stability, the preference for low pH, and the strong resistance to common salts make the MoO<sub>x</sub>-Pd/C catalyst suitable for degrading ClO<sub>3</sub><sup>-</sup> in waste brines in the chlor-alkali process and other scenarios such as water purification, environmental remediation, and waste brine valorization. This work shows great promise of exploring relatively abundant elements to expand the functionality of hydrogenation catalysts for environmental and energy applications. 48,49

#### MATERIALS AND METHODS

**Reagents and Materials.** Ultra-high-purity  $H_2$  gas (99.999%, Airgas), standard 2 N sulfuric acid solution (Alfa Aesar), POM precursors (Sigma-Aldrich or Alfa Aesar), and all other chemicals (Sigma-Aldrich or Fisher Scientific) were used as received. All aqueous solutions were prepared with deionized (DI) water (resistivity > 18.2 M $\Omega$  cm). The 5 wt % Pd/C (Sigma-Aldrich, catalog #330116, wet paste) was dried and treated prior to use as previously described.

Catalyst Preparation and Chlorate Reduction. For the preparation of a typical 0.2 g L<sup>-1</sup> loading of the MoO<sub>x</sub>-Pd/C catalyst containing nominally 5 wt % Mo, a 50 mL roundbottom flask was sequentially loaded with 50 mL of DI water (pH adjusted to 3.0 with 2N H<sub>2</sub>SO<sub>4</sub>), 10 mg of Pd/C powder, 0.5 mL of Na<sub>2</sub>MoO<sub>4</sub> stock solution (containing 0.5 mg Mo), and a magnetic stir bar. The flask was sealed with a rubber stopper and sonicated for 1 min to disperse the Pd/C in water. The aqueous suspension was stirred at 1600 rpm under 1 atm H<sub>2</sub> headspace for at least 15 min to allow the immobilization of Mo POM species onto the carbon support. The H<sub>2</sub> gas was supplied by two 16-gauge in diameter and 6-inch in length stainless steel needles as gas inlet and outlet to the fume hood. The catalytic reduction of a typical 1 mM ClO<sub>3</sub> was initiated by adding 0.25 mL of NaClO<sub>3</sub> stock solution (200 mM) into the catalyst suspension. For the initial ClO<sub>3</sub><sup>-</sup> concentration of 1 M, 5.32 g of solid NaClO<sub>3</sub> was added into the suspension. Aliquots were collected through the H<sub>2</sub> outlet needle with a 3 mL plastic syringe and immediately filtered through a 0.22  $\mu$ m cellulose membrane to quench reactions.

**Aqueous Sample Analysis.** The quantitation of  $ClO_3^-$ ,  $Cl^-$ ,  $BrO_3^-$ , and  $NO_3^-$  in aqueous samples was conducted by ion chromatography (Dionex ICS-5000 system with a conductivity detector and a 25  $\mu$ L sample injection loop). Brine samples were diluted 100 times before analysis. A Dionex IonPac AS19 analytical column was used to separate  $ClO_3^-$  from other anions. The most effective separation was achieved by maintaining the column at 30 °C and using 20 mM KOH at 1 mL min<sup>-1</sup> as the eluent. When Br<sup>-</sup> was present,  $ClO_3^-$  was

separated by an IonPac AS18 column at 30 °C with 16 mM KOH at 1 mL min<sup>-1</sup> as the eluent. The concentration of total Mo in aqueous samples was analyzed by inductively coupled plasma-mass spectrometry (ICP-MS, Agilent 7700).

Catalyst Collection and Characterization. After disconnection from the H2 supply, the catalyst suspension (the flask still being sealed by the rubber stopper) was quickly transferred into an anaerobic glove bag (Coy Laboratories, filled with 98% N2 and 2% H2) to avoid artifacts from air exposure. The catalyst suspension was filtered through a ceramic funnel covered with a filter paper (Whatman qualitative) under vacuum. The filter paper coated by the catalyst was transferred into a 20 mL scintillation vial. The vial was placed in a sand bath at 110 °C to remove moisture from the catalyst powder. The contents of Mo and Pd were measured by inductively coupled plasma-optical emission spectroscopy (ICP-OES, PerkinElmer Optima 8300) after digestion with HCl/HNO<sub>3</sub>. The surface area and pore structure were characterized by N<sub>2</sub> Brunauer-Emmett-Teller (BET) adsorption-desorption isotherms measured at 77 K using a Micromeritics ASAP 2020 analyzer. The surface area of Pd was determined by CO chemisorption. 50 The catalyst sample for microscopy analysis was redispersed in distilled water and sonicated for 30 min. A drop of the suspension was loaded onto the copper microgrids and dried under vacuum. The distribution of Mo, Pd, C, and O elements was characterized by high-angle annular dark-field (HAADF) imaging with scanning transmission electron microscopy (STEM, FEI Titan Themis 300, operated at 300 kV).

X-ray Photoelectron Spectroscopy (XPS). Inside the glove bag, the dried powder was loaded onto a copper conductive tape on the XPS sample holder and stored in an anaerobic chamber secured with Klein Flange for the transfer to the XPS facility. All XPS experiments were performed on the Kratos AXIS Supra surface analysis instrument at the UC Irvine Materials Research Institute (IMRI). The sp<sup>2</sup> C 1s peak (284.5 eV) of the carbon support was used for binding energy calibration. For Mo reference standards that were mixed with Nb<sub>2</sub>O<sub>5</sub> powder, the binding energy of Nb 3d<sub>5/2</sub> was set to 207.6 eV. The spectra in the resolution of 0.1 eV were fit using CasaXPS (version 2.3.19). The spectra of Pd 3d (collected with 5 scans), Mo 3d (30 scans), and Nb 3d (30 scans) were fit with the constrained peak separations (5.27 eV for Pd, 3.15 eV for Mo, and 2.75 eV for Nb) and the constrained ratio of peak areas (3:2) of 3d spin-orbital coupling doublets.

X-ray Absorption Spectroscopy (XAS). The preparation and transfer of XAS samples are the same as mentioned above. Mo K-edge EXAFS data were collected at beamlines 4-1 and 2-2 at the Stanford Synchrotron Radiation Light source. During the data collection, the sample chamber was purged with N<sub>2</sub> to minimize sample alteration by atmospheric O<sub>2</sub>. Both transmission signals and fluorescence signals were acquired. A Mo metal foil reference was concomitantly measured with the samples for energy calibration ( $E_0 = 20000$  eV). Zirconium (Z-2) metal foil was used as the filter for collecting fluorescence signals. Athena was used for energy calibration, raw spectra average, post-edge normalization, and background removal.<sup>51</sup> Artemis was used to obtain the structural parameters by fitting  $k^3$ -weighted EXAFS spectra to the standard EXAFS equation using several single-scattering paths. The fittings were over a k range of  $3-13 \text{ Å}^{-1}$  and an R range of 1.0-3.0 Å for the catalyst sample, a k range of  $3-12 \text{ Å}^{-1}$  and an R range of 1.2-3.9 Å for MoO<sub>2</sub> standard, and a k range of 3–12 Å<sup>-1</sup> and an R

range of 0.9-2.0 Å for  $(NH_4)_6Mo_7O_{24}$  standard. Phase and amplitude functions for the scattering paths were generated using FEFF6<sup>52</sup> based on the  $MoO_2$ ,  $MoO_3$ , and monomolybdate structures. In all fittings, the number of independent variables included was fewer than the number of independent data points. The Hanning window was used for the Fourier transform of the EXAFS data.

**Homogeneous Reaction.** In the anaerobic glove bag, a 15 mL glass reaction tube was loaded with 6 mL of water, 34.8 mg of sodium molybdate dihydrate, 60 μL of aqueous hydrazine solution (15.6 M), and a magnetic stir bar. The resulting aqueous solution thus contained 24 mM of Mo<sup>VI</sup> and 156 mM of  $\rm H_2N-NH_2$ . The solution pH was further adjusted to 3.0 with 1 N HCl. The tube was sealed with a Teflon screw cap and heated in a 70 °C oil bath for 24 h. Sodium chlorate (0.5 mM) was then added to monitor the  $\rm ClO_3^-$  reduction in the homogeneous solution for another 24 h at 70 °C. Aliquots of 1 mL solution were collected at time intervals. Each sample was diluted with another 1 mL of DI water before IC analysis.

#### ASSOCIATED CONTENT

# Supporting Information

The Supporting Information is available free of charge at https://pubs.acs.org/doi/10.1021/acscatal.0c02242.

Evaluation of mass transfer effects; results of alternative EXAFS fitting methods; concentration—time profiles for ClO<sub>3</sub><sup>-</sup>, BrO<sub>3</sub><sup>-</sup>, NO<sub>3</sub><sup>-</sup>, and dissolved Mo; additional XPS spectra (PDF)

# AUTHOR INFORMATION

## **Corresponding Author**

Jinyong Liu — Department of Chemical and Environmental Engineering, University of California, Riverside, California 92521, United States; ⊙ orcid.org/0000-0003-1473-5377; Email: jyliu@engr.ucr.edu, jinyong.liu101@gmail.com

# Authors

Changxu Ren — Department of Chemical and Environmental Engineering, University of California, Riverside, California 92521, United States; orcid.org/0000-0002-1109-794X

**Peng Yang** — Department of Ecosystem Science and Management, University of Wyoming, Laramie, Wyoming 82071, United States

Jinyu Gao — Department of Chemical and Environmental Engineering, University of California, Riverside, California 92521, United States; orcid.org/0000-0002-1751-3430

Xiangchen Huo — Department of Civil and Environmental Engineering, Colorado School of Mines, Golden, Colorado 80401, United States; orcid.org/0000-0002-7932-4563

Xiaopeng Min — Department of Civil and Environmental Engineering, University of Wisconsin-Milwaukee, Milwaukee, Wisconsin 53201, United States

Eric Y. Bi — Department of Chemical and Environmental Engineering, University of California, Riverside, California 92521, United States; Martin Luther King High School, Riverside, California 92508, United States

Yiming Liu — Department of Chemical and Environmental Engineering, University of California, Riverside, California 92521, United States

Yin Wang — Department of Civil and Environmental Engineering, University of Wisconsin-Milwaukee, Milwaukee, Wisconsin 53201, United States; o orcid.org/0000-0001-6723-7975

Mengqiang Zhu — Department of Ecosystem Science and Management, University of Wyoming, Laramie, Wyoming 82071, United States; orcid.org/0000-0003-1739-1055

Complete contact information is available at: https://pubs.acs.org/10.1021/acscatal.0c02242

#### Notes

The authors declare no competing financial interest.

# ACKNOWLEDGMENTS

Financial support was provided by the UCR faculty research startup grant (for J.L., C.R., and J.G.), the U.S. Department of Energy Experimental Program to Stimulate Competitive Research (DOE-EPSCOR DE-SC0016272, for P.Y. and M.Z.), the UWM faculty research startup grant (191502, for X.M. and Y.W.), and the National Science Foundation (CBET-1932942 for J.L. and CBET-1932908 for Y.W.). Y.L. thanks Tsinghua University for the undergraduate oversea research internship. Dr. Ruoxue Yan provided helpful discussions. Dr. Ich Tran is acknowledged for assistance in XPS characterization performed at the UC Irvine Materials Research Institute (IMRI) using instrumentation funded in part by the National Science Foundation Major Research Instrumentation Program under grant no. CHE-1338173.

#### REFERENCES

- (1) Karlsson, R. K.; Cornell, A. Selectivity between oxygen and chlorine evolution in the chlor-alkali and chlorate processes. *Chem. Rev.* **2016**, *116*, 2982–3028.
- (2) IMARC Group. Sodium Chlorate Market: Global Industry Trends, Share, Size, Growth, Opportunity and Forecast 2019–2024, 2019. https://www.researchandmarkets.com/reports/4763062 (accessed June 24, 2020).
- (3) EPA. Six-Year Review 3 Technical Support Document for Chlorate; (EPA-810-R-16-013); U.S. Environmental Protection Agency, Office of Water, 2016.
- (4) WHO. Chlorite and Chlorate in Drinking-Water: Background Document for Development of WHO Guidelines for Drinking-Water Quality; (WHO/SDE/WSH/05.08/86); World Health Organization, 2005.
- (5) U.S. Environmental Protection Agency. Revisions to the unregulated contaminant monitoring regulation (UCMR 3) for public water systems. *Fed. Regist.* **2012**, *77*, 26072–26101.
- (6) Brinkmann, T.; Santonja, G. G.; Schorcht, F.; Roudier, S.; Sancho, L. D. Best Available Techniques (BAT) Reference Document for the Production of Chlor-Alkali; Industrial Emissions Directive, 2010/75/EU (Integrated Pollution Prevention and Control); Publications Office of the European Union: Luxembourg, 2014.
- (7) Ibl, N.; Landolt, D. On the mechanism of anodic chlorate formation in dilute NaCl solutions. *J. Electrochem. Soc.* **1968**, *115*, 713–720
- (8) Landolt, D.; Ibl, N. On the mechanism of anodic chlorate formation in concentrated NaCl solutions. *Electrochim. Acta* **1970**, *15*, 1165–1183.
- (9) Macounová, K. M.; Simic, N.; Ahlberg, E.; Krtil, P. Electrocatalytic aspects of the chlorate process: A voltammetric and DEMS comparison of RuO<sub>2</sub> and DSA anodes. *J. Electrochem. Soc.* **2018**, *165*, E751–E758.
- (10) Lakshmanan, S.; Murugesan, T. Adsorption performance of coconut shell activated carbon for the removal of chlorate from chloralkali brine stream. *Water Sci. Technol.* **2016**, *74*, 2819–2831.
- (11) Van Santen, R.; Klesing, A.; Neuenfeldt, G.; Ottmann, A. Method for removing chlorate ions from solutions. U.S. Patent US6,270,6822001.

- (12) Park, H.; Vecitis, C. D.; Hoffmann, M. R. Electrochemical water splitting coupled with organic compound oxidation: The role of active chlorine species. *J. Phys. Chem. C* **2009**, *113*, 7935–7945.
- (13) Cho, K.; Qu, Y.; Kwon, D.; Zhang, H.; Cid, C. M. A.; Aryanfar, A.; Hoffmann, M. R. Effects of anodic potential and chloride ion on overall reactivity in electrochemical reactors designed for solar-powered wastewater treatment. *Environ. Sci. Technol.* **2014**, *48*, 2377–2384.
- (14) Kumar, A.; Phillips, K. R.; Thiel, G. P.; Schröder, U.; Lienhard, J. H. Direct electrosynthesis of sodium hydroxide and hydrochloric acid from brine streams. *Nat. Catal.* **2019**, *2*, 106–113.
- (15) Chen, X.; Huo, X.; Liu, J.; Wang, Y.; Werth, C. J.; Strathmann, T. J. Exploring beyond palladium: Catalytic reduction of aqueous oxyanion pollutants with alternative platinum group metals and new mechanistic implications. *Chem. Eng. J.* 2017, 313, 745–752.
- (16) Kuznetsova, L. I.; Kuznetsova, N. I.; Koscheev, S. V.; Zaikovskii, V. I.; Lisitsyn, A. S.; Kaprielova, K. M.; Kirillova, N. V.; Twardowski, Z. Carbon-supported iridium catalyst for reduction of chlorate ions with hydrogen in concentrated solutions of sodium chloride. *Appl. Catal., A* **2012**, *427*, 8–15.
- (17) Liu, J.; Chen, X.; Wang, Y.; Strathmann, T. J.; Werth, C. J. Mechanism and mitigation of the decomposition of an oxorhenium complex-based heterogeneous catalyst for perchlorate reduction in water. *Environ. Sci. Technol.* **2015**, *49*, 12932–12940.
- (18) Wang, S.-S.; Yang, G.-Y. Recent advances in polyoxometalate-catalyzed reactions. *Chem. Rev.* **2015**, *115*, 4893–4962.
- (19) Kolthoff, I. Jodometrische Studien (Schluss). Z. Anal. Chem. 1921, 60, 448-457.
- (20) Kolthoff, I.; Hodara, I. Polarographic study of the molybdenum catalyzed reduction of chlorate, perchlorate and nitrate. *J. Electroanal. Chem.* **1963**, *5*, 2–16.
- (21) Masters-Waage, N. K.; Morris, K.; Lloyd, J. R.; Shaw, S.; Mosselmans, J. F. W.; Boothman, C.; Bots, P.; Rizoulis, A.; Livens, F. R.; Law, G. T. Impacts of repeated redox cycling on technetium mobility in the environment. *Environ. Sci. Technol.* **2017**, *51*, 14301–14310.
- (22) Wang, L.; Song, H.; Yuan, L.; Li, Z.; Zhang, P.; Gibson, J. K.; Zheng, L.; Wang, H.; Chai, Z.; Shi, W. Effective removal of anionic Re (VII) by surface-modified  ${\rm Ti_2CT_x}$  MXene nanocomposites: Implications for Tc (VII) sequestration. *Environ. Sci. Technol.* **2019**, *53*, 3739–3747.
- (23) Choe, J. K.; Shapley, J. R.; Strathmann, T. J.; Werth, C. J. Influence of rhenium speciation on the stability and activity of Re/Pd bimetal catalysts used for perchlorate reduction. *Environ. Sci. Technol.* **2010**, *44*, 4716–4721.
- (24) Choe, J. K.; Boyanov, M. I.; Liu, J.; Kemner, K. M.; Werth, C. J.; Strathmann, T. J. X-ray spectroscopic characterization of immobilized rhenium species in hydrated rhenium–palladium bimetallic catalysts used for perchlorate water treatment. *J. Phys. Chem. C* 2014, *118*, 11666–11676.
- (25) Oyerinde, O. F.; Weeks, C. L.; Anbar, A. D.; Spiro, T. G. Solution structure of molybdic acid from Raman spectroscopy and DFT analysis. *Inorg. Chim. Acta* **2008**, *361*, 1000–1007.
- (26) McAdam, E.; Judd, S. Biological treatment of ion-exchange brine regenerant for re-use: A review. *Sep. Purif. Technol.* **2008**, *62*, 264–272.
- (27) Clark, C. A.; Reddy, C. P.; Xu, H.; Heck, K. N.; Luo, G.; Senftle, T. P.; Wong, M. S. Mechanistic Insights into pH-controlled nitrite reduction to ammonia and hydrazine over rhodium. *ACS Catal.* **2019**, *10*, 494–509.
- (28) Liu, B. Y.; Wagner, P. A.; Earley, J. E. Reduction of perchlorate ion by (N-(hydroxyethyl) ethylenediaminetriacetato) aquatitanium (III). *Inorg. Chem.* **1984**, 23, 3418–3420.
- (29) Hurley, K. D.; Shapley, J. R. Efficient heterogeneous catalytic reduction of perchlorate in water. *Environ. Sci. Technol.* **2007**, 41, 2044–2049.
- (30) Liu, J.; Choe, J. K.; Sasnow, Z.; Werth, C. J.; Strathmann, T. J. Application of a Re-Pd bimetallic catalyst for treatment of

- perchlorate in waste ion-exchange regenerant brine. Water Res. 2013, 47, 91–101.
- (31) Sanz, J.; Hofmann, S. Auger electron spectroscopy and X-ray photoelectron spectroscopy studies of the oxidation of polycrystalline tantalum and niobium at room temperature and low oxygen pressures. *J. Less-Common Met.* **1983**, 92, 317–327.
- (32) Iyer, A. K.; Peter, S. C. Two-dimensional bicapped supramolecular hybrid semiconductor material constructed from the insulators  $\alpha$ -Keggin polyoxomolybdate and 4, 4'-bipyridine. *Inorg. Chem.* **2013**, 53, 653–660.
- (33) Haushalter, R. C.; Mundi, L. A. Reduced molybdenum phosphates: octahedral-tetrahedral framework solids with tunnels, cages, and micropores. *Chem. Mater.* **1992**, *4*, 31–48.
- (34) Choi, J.-G.; Thompson, L. XPS study of as-prepared and reduced molybdenum oxides. *Appl. Surf. Sci.* **1996**, 93, 143–149.
- (35) Wang, H.; Hamanaka, S.; Nishimoto, Y.; Irle, S.; Yokoyama, T.; Yoshikawa, H.; Awaga, K. In operando X-ray absorption fine structure studies of polyoxometalate molecular cluster batteries: polyoxometalates as electron sponges. *J. Am. Chem. Soc.* **2012**, *134*, 4918–4924.
- (36) Jalilehvand, F.; Lim, B. S.; Holm, R.; Hedman, B.; Hodgson, K. O. X-ray absorption spectroscopy of a structural analogue of the oxidized active sites in the sulfite oxidase enzyme family and related molybdenum (V) complexes. *Inorg. Chem.* **2003**, *42*, 5531–5536.
- (37) Brandt, B. G.; Skapski, A. A refinement of the crystal structure of molybdenum dioxide. *Acta Chem. Scand.* **1967**, *21*, 661–672.
- (38) Wang, Y.; Weinstock, I. A. Polyoxometalate-decorated nanoparticles. *Chem. Soc. Rev.* **2012**, *41*, 7479–7496.
- (39) Maksimovskaya, R. I. Molybdophosphate heteropoly blues: Electron-transfer reactions in aqueous solutions as studied by NMR. *Polyhedron* **2013**, *65*, 54–59.
- (40) Wee, H.-Y.; Cunningham, J. A. Palladium-catalyzed hydrodehalogenation of 1, 2, 4, 5-tetrachlorobenzene in water—ethanol mixtures. *J. Hazard. Mater.* **2008**, *155*, 1–9.
- (41) Borgschulte, A.; Sambalova, O.; Delmelle, R.; Jenatsch, S.; Hany, R.; Nüesch, F. Hydrogen reduction of molybdenum oxide at room temperature. *Sci. Rep.* **2017**, *7*, No. 40761.
- (42) Liu, J.; Choe, J. K.; Wang, Y.; Shapley, J. R.; Werth, C. J.; Strathmann, T. J. Bioinspired complex-nanoparticle hybrid catalyst system for aqueous perchlorate reduction: Rhenium speciation and its influence on catalyst activity. *ACS Catal.* **2014**, *5*, 511–522.
- (43) Sugimoto, H.; Tsukube, H. Chemical analogues relevant to molybdenum and tungsten enzyme reaction centres toward structural dynamics and reaction diversity. *Chem. Soc. Rev.* **2008**, *37*, 2609–2619.
- (44) Elrod, L. T.; Kim, E. Lewis acid assisted nitrate reduction with biomimetic molybdenum oxotransferase complex. *Inorg. Chem.* **2018**, *57*, 2594–2602.
- (45) Reeds, J. P.; Yonke, B. L.; Zavalij, P. Y.; Sita, L. R. Carbon monoxide-induced N–N bond cleavage of nitrous oxide that is competitive with oxygen atom transfer to carbon monoxide as mediated by a Mo (II)/Mo (IV) catalytic cycle. *J. Am. Chem. Soc.* **2011**, *133*, 18602–18605.
- (46) Schindler, T.; Sauer, A.; Spaniol, T. P.; Okuda, J. Oxygen atom transfer reactions with molybdenum cofactor model complexes that contain a tetradentate OSSO-type bis(phenolato) ligand. *Organometallics* **2018**, *37*, 4336–4340.
- (47) Kuznetsova, L.; Kuznetsova, N. Cyclohexane oxidation with an  $O_2$ - $H_2$  mixture in the presence of a two-component Pt/C-heteropoly acid catalyst and ionic liquids. *Kinet. Catal.* **2017**, *58*, 522–532.
- (48) Chaplin, B. P.; Reinhard, M.; Schneider, W. F.; Schüth, C.; Shapley, J. R.; Strathmann, T. J.; Werth, C. J. Critical review of Pdbased catalytic treatment of priority contaminants in water. *Environ. Sci. Technol.* **2012**, *46*, 3655–3670.
- (49) Yin, Y. B.; Guo, S.; Heck, K. N.; Clark, C. A.; Coonrod, C. L.; Wong, M. S. Treating water by degrading oxyanions using metallic nanostructures. ACS Sustainable Chem. Eng. 2018, 6, 11160–11175.

- (50) Huo, X.; Liu, J.; Strathmann, T. J. Ruthenium catalysts for the reduction of N-nitrosamine water contaminants. *Environ. Sci. Technol.* **2018**, *52*, 4235–4243.
- (51) Ravel, B.; Newville, M. ATHENA, ARTEMIS, HEPHAESTUS: Data analysis for X-ray absorption spectroscopy using IFEFFIT. *J. Synchrotron Radiat.* **2005**, *12*, 537–541.
- (52) Zabinsky, S.; Rehr, J.; Ankudinov, A.; Albers, R.; Eller, M. Multiple-scattering calculations of X-ray-absorption spectra. *Phys. Rev. B* **1995**, *52*, 2995–3009.